Accepted Manuscript

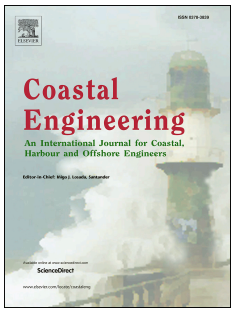

Wake effect assessment of a flap type wave energy converter farm under realistic environmental conditions by using a numerical coupling methodology

Nicolas Tomey-Bozo, Aurélien Babarit, Jimmy Murphy, Vicky Stratigaki, Peter Troch, Tony Lewis, Gareth Thomas

PII: S0378-3839(17)30554-9

DOI: https://doi.org/10.1016/j.coastaleng.2018.10.008

Reference: CENG 3436

To appear in: *Coastal Engineering*

Received Date: 6 October 2017

Revised Date: 11 July 2018

Accepted Date: 20 October 2018

Please cite this article as: Tomey-Bozo, N., Babarit, Auré., Murphy, J., Stratigaki, V., Troch, P., Lewis, T., Thomas, G., Wake effect assessment of a flap type wave energy converter farm under realistic environmental conditions by using a numerical coupling methodology, *Coastal Engineering* (2018), doi: https://doi.org/10.1016/j.coastaleng.2018.10.008.

This is a PDF file of an unedited manuscript that has been accepted for publication. As a service to our customers we are providing this early version of the manuscript. The manuscript will undergo copyediting, typesetting, and review of the resulting proof before it is published in its final form. Please note that during the production process errors may be discovered which could affect the content, and all legal disclaimers that apply to the journal pertain.

ACCEPTED MANUSCRIPT

Wake effect assessment of a flap type wave energy converter farm under realistic environmental conditions by using a numerical coupling methodology

Nicolas Tomey-Bozo[a,*], Aurélien Babarit[b], Jimmy Murphy[a], Vicky Stratigaki[c], Peter Troch[c], Tony Lewis[a], Gareth Thomas[d]

[a] *MaREI Centre (ERI), University College Cork, Haulbowline Road, Ringaskiddy, Ireland*
[b] *Ecole Centrale de Nantes CNRS, 1 rue de la Noé, 44300 Nantes, France*
[c] *Department of Civil Engineering, Ghent University, Zwijnaarde, Belgium*
[d] *School of Mathematical Sciences, University College Cork, Cork, Ireland*

Abstract

Ocean Energy Europe has estimated that 100 GW of ocean energy capacity (wave and tidal) could be deployed in Europe by 2050. Along with the European targets it is expected that large farms of Wave Energy Converters (WECs) will be installed in the sea and, as part of the consenting process for their installation, it will be necessary to quantify their impact on the local environment. The objective of this study is to improve the assessment of WEC farms impact on the surrounding wave field (wake effect) through the use of a numerical coupling methodology. The methodology consists of a Boundary Element Method (BEM) solver to obtain the wave perturbation generated by the WEC farm for the near-field accounting for the wave-body interactions within the farm whilst a Wave Propagation Model (WPM) based on the mild-slope equations determines the wave transformation in the far-field. The near-field solution obtained from the BEM solver is described as an internal boundary condition in the WPM and then it is propagated throughout the WPM numerical domain. The internal boundary is described by imposing the solution of the surface elevation and velocity potential at the free-surface at each instant of time along a line surrounding the WEC farm.

As a case study the methodology was applied to flap type WECs that are deployed in shallow water conditions. The validation of the technique was done first for a single flap and then for a farm of 5 flaps. Once validated, a realistic scenario was assessed by quantifying the impact of irregular sea states composed of long crested waves on a large WEC farm composed of 18 flaps and located on a real bathymetry. The irregular waves were obtained by superposing the regular wave field solutions for all wave frequencies represented in the considered sea state based on the linear water wave theory. Within the limits of this theory

*Corresponding author
Email address: nicolas.tomey@ucc.ie (Nicolas Tomey-Bozo)

ACCEPTED MANUSCRIPT

these simulations demonstrate the versatility of the methodology to accurately represent the impact of a WEC farm on the surrounding wave climate. The influence of the peak period and the spacing between flaps on the WEC farm wake effect was assessed as well.

Keywords: Wave Energy Converter, Wake Effect, Wave Propagation, Wave Farm, Coupling Methodology
2010 MSC: 00-01, 99-00

1. Introduction

The presence of Wave Energy Converter (WEC) farms in the ocean will locally affect the wave climate. WECs are designed to absorb part of the incoming wave energy and therefore to reduce the amount of energy density in the lee side of the farm (wake effect). The quantification of the wake effect generated by a WEC farm is an important consideration in the consenting process for the deployment of these technologies. Furthermore, their potential capability to have a sheltering effect on other marine activities taking place in the lee of the farm may open various opportunities. For these reasons this study aims to improve the state of the art of the methodologies to quantify the wake effect generated by a WEC farm.

Some studies have used Wave Propagation Models (WPMs) to assess the far-field effect on the lee side of a WEC farm [1, 2, 3, 4, 5, 6, 7, 8, 9, 10] by representing intrinsically the devices as absorption cells or source terms. Others have assessed the near-field wave interactions between devices by using Boundary Element Method (BEM) solvers [11, 12]. References [13, 14] summarise and describe in detail all types techniques that have attempted to address this problem. WPMs are accurate solvers of the wave propagation throughout large domains considering realistic conditions such as irregular bathymetries and dissipative processes. However, these models do not accurately represent the local wave-body interactions and rely on external lookup tables describing the absorption capacity of the WECs in order to represent them inherently. BEM solvers are the opposite as they provide accurate solutions of the local wave-body interaction phenomena by solving the well-known boundary value problem but are limited in terms of the constant depth assumptions and the restricted-size numerical domains.

A coupling methodology is applied in this study to bridge the gap between the near-field results obtained from a BEM solver and the wave propagation in the far-field solved in a WPM based on the mild-slope equations. In previous studies such as those by [15, 16, 17, 18, 19, 20] similar coupling methodologies have been developed for point absorber WECs or surging barges for regular wave cases. In this study an improved methodology that uses a coupling technique which has applications to irregular sea states composed of long crested waves is presented. An internal boundary condition is described within the WPM for each regular wave frequency based on the perturbed wave field solution obtained from the BEM solver. The propagation of the perturbed wave is then solved

ACCEPTED MANUSCRIPT

throughout the rest of the domain within the WPM. The superposition of the two separated calculations, the perturbed wave field solved by applying the coupling technique and the incident wave field computed intrinsically, allows the computation of the total wave field for each frequency. The application of the methodology to a farm of various WECs and the superposition of the regular wave field solutions enables the assessment of WEC farm wake effects for realistic scenarios.

This paper presents an extension of the recent work published by the same authors in [21] where a preliminary version of the methodology was described. This study starts with the description of the numerical tools employed and their main governing equations. The proposed methodology is then outlined by describing the technical set up of the internal boundary that allows for the coupling between the two solvers. The coupling technique is validated first for a single-WEC case consisting of a flap type device, and then for a WEC farm composed of 5 devices. In order to validate the methodology the results are compared against BEM solver results by assuming constant water depths and error plots are then computed for both cases. A convergence analysis is carried out to assess the influence of the main numerical parameters on the results and define their optimum values. Then the wake effects for a large WEC farm composed of a large number of devices and located on a real bathymetry is computed for irregular long crested waves in order to demonstrate the versatility of the methodology when considering real environmental conditions. The influence on the wake effect of the peak period for the considered sea state and the influence of the spacing between flaps are assessed as well.

2. Literature Review

The first work to apply a similar coupling technique to WECs was Reference [15]. The BEM commercial solver WAMIT®[22] was used to solve the near-field surrounding the device and MILDwave was used as WPM for the calculation of the far-field results. The internal boundary condition describing the near-field solution in MILDwave was described as a circular wave generation line based on the source term addition method from Equation (17) together with an inner sponge layer. The methodology was applied to point absorbers and each device was represented in MILDwave as an single internal boundary. Regular wave results were obtained for a farm of several devices and thus the interactions were calculated within the WPM by means of superposing each wave component.

As a continuation to this work, Reference [16] focused on the improvement of the angle discretisation of the circular wave generation line and the validation against pure BEM solver solutions. Good agreements were found but due to the reflection caused by the inner sponge layer (sponge layer used within the circular wave generation line) it was difficult to obtain completely consistent reference values for the angle discretisation of the circular wave generation line. The author of the current work applied later the same coupling technique to a flap type WEC in [23] and compared the wave field results against the sponge layer technique where the WEC is modelled intrinsically within the WPM as an

ACCEPTED MANUSCRIPT

obstacle. The same small inconsistencies related with the inner sponge layer reflection were found needing to tune the angle discretisation each time a different radius was used for the internal boundary.

The previous aforementioned studies led to more recent works were coupling methodologies have been progressively improved and applied to more complex scenarios making use of different types of solvers. References [9, 21, 24, 25] presented different cases of coupling techniques between the BEM solver NEMOH [26] and MILDwave [27, 19], a WPM based on the mild-slope equations. These studies were applied to point absorber and flap type WEC farms under regular waves and mild-slope bathymetries. The coupling technique applications were based on a description of the near-field perturbation generated by the WEC as an internal boundary where the solution from NEMOH is imposed at the boundary in MILDwave, and therefore there is no need of an inner sponge layer. Then References [28, 29] presented a coupling technique between NEMOH and OceanWave3D [30] to point absorber type WEC farms composed of up to 5 devices and where irregular waves scenarios and changing depth bathymetries were considered for medium-scale domains. Result comparisons with the coupling technique between NEMOH and MILDwave and experimental data were undertaken showing very good agreements. Finally, references [31, 32] presented a coupling technique application between an SPH (Smooth Particle Hydrodynamics) solver and OceanWave3D for points absorber type WECs under regular waves.

References [17] and [18] adopted a similar coupling methodology between the BEM solver Aquaplus [33] (NEMOH nowadays) and the ARTEMIS module of Open TELEMAC-MASCARET [34], an open-source WPM. The Kochin function approximation was used to describe the fictitious island describing the wave perturbation generated by the WECs in the WPM. The methodology was applied to a farm of point absorber WECs under regular waves. The WECs were represented in ARTEMIS as individually separated internal boundary conditions and the interactions were computed within the WPM.

More recently Reference [20] developed a methodology where the so-called direct matrix method was adapted to the elliptic mild-slope equation. Based on a finite-element method the mild-slope equations were used to solve the effect of the bottom on the waves while the effect of the bodies was represented my means of the diffraction transfer matrices. The method was applied to solve regular waves solutions surrounding truncated vertical cylinders and surging barges that were compared against analytical solutions. The results are promising but the application cases are limited to regular waves.

In this study a one-directional coupling approach per regular wave solution is suggested between the BEM solver NEMOH [26] and the WPM MILDwave [27, 19] where an innovative set-up for the internal boundary is proposed. The methodology is applied to large WEC farms and then complex scenarios replicating real environmental conditions such as irregular sea states, large WEC farms, large domains, and real bathymetry scenarios, are computed in order to showcase the potential applications of the methodology. The internal boundary is defined by a wave generation line which implies that all cells along the

ACCEPTED MANUSCRIPT

line have a solution imposed based on the BEM solver results at the same location. The whole farm is computed within the BEM solver accounting for all interactions between devices and then the perturbed wave solution for the farm is propagated within the WPM. The versatility of the method is proven by adapting the internal boundary in the WPM to the shape of the WEC farm.

3. Numerical Tools Employed

Two main phenomena dominate in terms of the wake effect of a WEC farm: the wave-body interaction phenomena (near-field wave pattern) and the wave propagation throughout the rest of the numerical domain (far-field wave pattern). BEMs are selected as an appropriate tool to assess the local wave-body interaction in the near-field due to their high ratio of accuracy to computational time. These solvers are based on linear potential flow theory, thus while remaining below the assumption of this theory they provide an accurate representation of the wave field surrounding a wave energy converter by solving the scattering problem. There exist solvers that represent the wave perturbation with high accuracy even above the limits of the linear wave theory such as Computational Fluid Dynamics (CFD) solvers but their extremely high computational time demand makes them unsuitable for the application cases presented in this work.

The far-field wave pattern was obtained using a phase-resolving WPM based on the mild-slope equations. These models solve wave-by-wave the propagation of linear water waves in the time domain accounting for the main transformation processes. Some models include dissipative processes such as bottom friction and wave breaking. Coupling the solution from the BEM for the near-field remains theoretically a feasible task due to the similarity in the governing equations between the two solvers. The two hydrodynamic solvers are described in the following section together with the governing equations of the problems assessed.

3.1. Linear wave theory

The two models employed in this study are based on the linear wave theory and the applicability of this theory relies on the assumption that we remain within its limits of application. The linear wave theory assumptions are that:

- The fluid is inviscid
- The flow is irrotational, meaning $\nabla \times V = 0$.
- The fluid is incompressible, leading to the continuity equation expressed as $\nabla \cdot V = 0$.

where the irrotationality condition allows describing the flow velocity V as the gradient of the velocity potential ϕ described by Equation (1):

$$V(x, y, z) = \nabla\phi \tag{1}$$

ACCEPTED MANUSCRIPT

Equation 1 together with the incompressibility condition leads to the Laplace Equation:

$$\nabla^2 \phi = 0 \tag{2}$$

Seeking for a solution of the surface elevation $\eta(x, y, t)$ and velocity potential $\phi(x, y, z, t)$, a group of linearised boundary conditions at the free-surface and sea bottom are described assuming the wave amplitude is small with respect to the wavelength and water depth. The bottom condition ($z = -h(x, y)$) is given by Equation (3), and Equations (4) and (5) describe the kinematic and dynamic condition at the undisturbed free-surface ($z = 0$):

$$\frac{\partial \phi}{\partial z} = 0 \tag{3}$$

$$\frac{\partial \eta}{\partial t} = \frac{\partial \phi}{\partial z} \tag{4}$$

$$\frac{\partial \phi}{\partial t} + g\eta = 0 \tag{5}$$

where g represents the gravitational acceleration and the relation between η and ϕ is given by Equation (6)

$$\tilde{\eta}(x, y) = \frac{i\omega}{g} \tilde{\Phi}(x, y) \tag{6}$$

with Φ being the velocity potential ϕ at the free-surface condition ($z = 0$), overbar ($\tilde{}$) representing the complex form of the variable, and ω the angular wave frequency.

3.2. Open-source BEM solver NEMOH

NEMOH is an open-source BEM solver developed by Ecole Centrale de Nantes and is used in this work to obtain the near-field surrounding the WECs. NEMOH obtains the perturbed velocity potential as a 3D solution in the frequency domain from the linear wave-body interaction boundary value problem (or wave scattering problem) assuming constant water depth conditions. The wave scattering problem solves Laplace's equation (Equation (2)) assuming a set of boundary conditions composed of the bottom and free-surface boundary conditions described earlier in Equations (3), (4), and (5), and the body and scattering boundary conditions described next by Equations (7) and (8) respectively:

$$\frac{\partial \phi}{\partial n} = U \cdot n \tag{7}$$

$$\lim_{r \to +\infty} \phi_p = 0 \tag{8}$$

ACCEPTED MANUSCRIPT

where ϕ_p represents the perturbed velocity potential generated by the presence of the body, U the velocity of the body when it is assumed to be rigid, n the normal vector to the body surface, and where $r^2 = (x^2 + y^2)$. The body boundary condition needs to be satisfied at the wetted surface of the body for its undisturbed position, describing the non-porosity of the body surface. The scattering boundary condition describes the complete dispersion of the perturbed velocity potential at the infinity of the domain.

The wave scattering problem is divided into one diffraction problem and one radiation problem per degree of freedom of the body motion. Both problems are solved individually for each wave frequency using the Green's function. From the resolution of these problems the diffracted velocity potential ϕ_d and radiated velocity potential ϕ_r are obtained, and the sum of the two solutions gives the perturbed velocity potential ϕ_p.

The diffraction problem is computed considering the body is fixed under the presence of an incoming incident wave velocity potential ϕ_i described by Equation (9) at the infinity of the domain and the boundary condition from Equation (10) at the body surface:

$$\tilde{\phi_i}(x, y, z) = -\frac{ig}{\omega} A f_0(z) e^{(i(k(x\cos\beta + y\sin\beta) - \omega t - \varphi))} \tag{9}$$

$$\frac{\partial \phi_d}{\partial n} = -\frac{\partial \phi_i}{\partial n} \tag{10}$$

where A is the corresponding incident wave amplitude, $f_0(z)$ is the depth dependence, k the wave number related to the wavelength by $k = 2\pi/\lambda$, and β the angle of propagation direction with respect to the X axis.

Then the radiation problem is solved by considering a forced motion of the body in calm conditions (absence of waves) assuming the boundary condition from Equation (11) for the body surface and assuming the amplitude of the body motion is small with respect to its characteristic length:

$$\frac{\partial \phi_{r,j}}{\partial n} = U_j \cdot n_j \tag{11}$$

where j represents each degree of freedom of the body motion.

In order to clarify the way a BEM solver computes the perturbed wave Figure 1 shows a sketch representation of the scattering problem with the diffraction problem on top and the radiation problem bellow.

Using the principle of superposition the velocity potential for the total wave field ϕ_t in Equation (12) is calculated as a sum of the incident velocity potential described in Equation (9), and the diffracted and radiated velocity potential:

$$\tilde{\phi_t}(x, y, z) = \tilde{\phi_i} + \tilde{\phi_d} + \sum_{j=1}^{6} \tilde{\phi_{r,j}} \tag{12}$$

Then from the velocity potential at the free-surface condition ($z = 0$) it is straightforward to obtain the surface elevation for the total wave field from Equation (6).

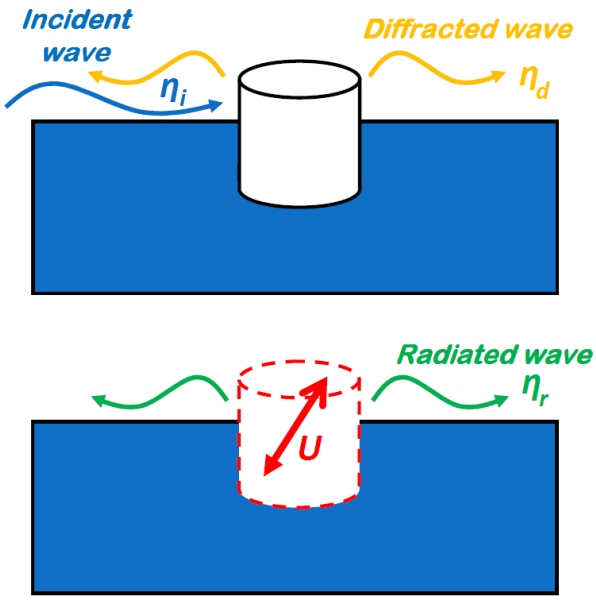

Figure 1: Sketch representation of the diffraction problem (top) and radiation problem (bottom).

3.3. Wave propagation model MILDwave

MILDwave is used in this study to solve the wave transformation processes throughout large domains and obtain the far-field wave pattern to assess the WEC farm wake effect. MILDwave is a time-dependent mild-slope equation model developed by Ghent University and is a phase-resolving type WPM. The model solves the propagation of surface waves throughout the domain and the interaction with obstacles (previously defined) by solving the depth-integrated mild-slope equations of Radder and Dingemans [35] (Equations (13) and (14)). These equations describe the transformation of linear regular and irregular waves with a narrow frequency band over a mild slope bathymetry (bed steepness up to 1/3 [36]):

$$\frac{\partial \eta}{\partial t} = B_c \Phi - \nabla(A_c \nabla \Phi) \tag{13}$$

$$\frac{\partial \Phi}{\partial t} = -g\eta \tag{14}$$

η and Φ represent respectively the surface elevation and velocity potential at the free-surface level, t represents the time, and g is the gravitational acceleration. The values of B_c and A_c are calculated using Equations (15) and (16):

ACCEPTED MANUSCRIPT

$$B_c = \frac{\omega^2 - k^2 C C_g}{g} \tag{15}$$

$$A_c = \frac{C C_g}{g} \tag{16}$$

with the phase velocity C and the group velocity C_g. The complete derivation of these equations can be found in [15].

A finite difference scheme is used to discretise and solve Equations (13) and (14) which consists of a two-step space-centred and time-staggered computational grid. The domain is divided in grid cells with dimensions Δx and Δy and central differences are used for spatial as well as time derivatives. Both η and Φ are calculated in the centre of each grid cell at different time levels, $(n + \frac{1}{2})\Delta t$ and $(n+1)\Delta t$ respectively, where Δt is the time step and n represents the step cycle.

Incident waves are generated in MILDwave at the offshore boundary by using the source term addition method, i.e. by adding an additional surface elevation η^* to the calculated value on a wave generation line for each time step given by Equation (17) as described in [37]:

$$\eta^* = 2\eta_i \frac{C_e \Delta t}{\Delta x} \sin\beta \tag{17}$$

with η_i the water surface elevation of incident waves derived from Equation (6) and (9), Δx the grid cell size in X direction, and C_e the energy velocity. The wave generation line is assumed to be parallel to the Y axis.

4. Flap Type Wave Energy Converter

4.1. Flap description

The flap type WEC is the technology to which the case scenarios are applied since it is a type of WEC perturbing significantly the incoming wave field and thus an appropriate application case to validate the methodology. The flap type WEC is defined as a surface-piercing flap hinged at the bottom of the seabed as shown in Figure 2. The motion is restricted to pitch therefore only one degree of freedom is considered. The shaft about which the flap rotates is at the base of the device. Table 1 shows the main characteristics of the flap where the relative density ρ_r defines the density of the WEC compared to the water density. The thickness t is not represented in the sketch since it has a small value compare to the rest of dimensions.

4.2. Flap dynamic modelling

The amplitudes of rotation for each flap are calculated based on Equation (18) for each angular wave frequency ω. The hydrodynamic coefficients Γ, A_r and B_r, are obtained from NEMOH where Γ represents the excitation force coefficient, and A_r and B_r are the radiation added inertia and radiation damping

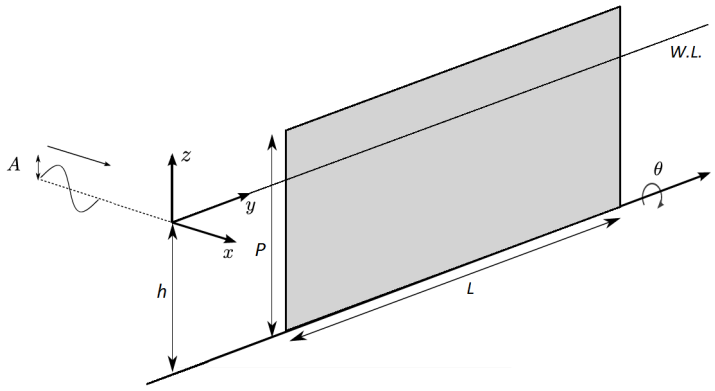

Figure 2: Sketch representation of the flap type WEC

Table 1: Main characteristics of the flap type WEC.

Parameter	Coefficient	Value	Units
Length	L	20	m
Height	P	12	m
Thickness	t	1	m
Relative density	ρ_r	0.3	-

coefficients. The hydrostatic coefficient H and the moment of inertia I are calculated based on the geometry description from Table (1). The Power Take Off (PTO) damping coefficient B_{PTO} is calculated based on Equation (19).

$$\Theta(\omega) = \frac{A\Gamma(\omega)}{-\omega^2(I + A_r(\omega)) - i\omega(B_r(\omega) + B_{PTO}) + H} \tag{18}$$

The resultant values of the rotation amplitude are used to quantify the radiated wave solution obtained from NEMOH, which is first obtained in a non-dimensional form relative to a unit of rotation amplitude (see Section 5.2). In the case of a farm where various WECs are considered within the BEM solver, the terms composing Equation (18) are expanded to j dimensions where j represents the number of degrees of freedom of body motion (one per device in this case). The expanded form of the equation of motion takes account of all interactions between WECs and therefore determines the rotation amplitude for each device whilst the presence of the surrounding moving devices.

A passive PTO composed of a damper is used in this study. This configuration was chosen to represent a hydraulic PTO which is usually employed for the flap type WECs. Equation (19) defines the optimum value of the PTO damping

ACCEPTED MANUSCRIPT

coefficient for a specific wave frequency which is theoretically demonstrated in [38]. In the case of an irregular sea state composed of many wave frequencies a fixed value of the PTO damping coefficient was assigned considering the overall statistics of the sea state instead of an optimal value for each frequency that would be constantly changing in time. Thus, the peak angular wave frequency ω_p of the considered sea state is applied as a fixed optimum value.

$$B_{PTO} = \sqrt{\left(\frac{H}{\omega_p} - \omega(I + A_r(\omega_p))\right)^2 + B_r(\omega_p)^2} \tag{19}$$

5. Methodology

5.1. General approach

The methodology is applied to regular waves that are then post-processed to obtain the corresponding irregular sea state based on a considered incident wave spectrum. Each regular wave solution is composed of an incident wave and a perturbed wave solution that are superposed to obtain the total wave. As a first step the incident wave is solved intrinsically in MILDwave by means of a wave generation line located at the up-wave side of the domain that allows the wave to propagate towards the X positive axis. The incident wave is generated by using the usual source term addition method from Equation (17). As a separated calculation, the perturbed wave is obtained by means of a coupling technique that merges the near-field results surrounding the WEC farm from NEMOH into MILDwave as an internal boundary condition that allows for the propagation of the wave towards the rest of the domain.

The perturbed wave is quantified based on the amplitude obtained for the incident wave calculation at the centre of the WEC farm ($X = 0$ m and $Y = 0$ m) and both are synchronised in phase, considering the reference of the incident wave phase been 0 at the same location. Figure 3 shows a sketch of the methodology representing both calculations, the perturbed wave and the incident wave.

5.2. Coupling technique description

The internal boundary condition is described in this work as a wave generation line where the solution obtained from the BEM solver is imposed at each grid cell along the line surrounding all devices from the WEC farm. As described in Section 3.3, MILDwave solves the instantaneous surface elevation and the velocity potential at the free-surface for each instant of time. Thus, these two variables are imposed along the wave generation line (black doted line in Figure 4) at each time step in order to propagate the wave towards the far-field. The near-field solution is given by the BEM solver and the far-field solution is given by the WPM, as illustrated by Figure 4.

The perturbed wave field solution is obtained from NEMOH in the frequency-domain in terms of wave amplitude A_N and phase φ_N. These are then transformed by Equations (20) and (21) into the time-domain variables η_{MW} and Φ_{MW} to be imposed in MILDwave at each instant of time at the internal

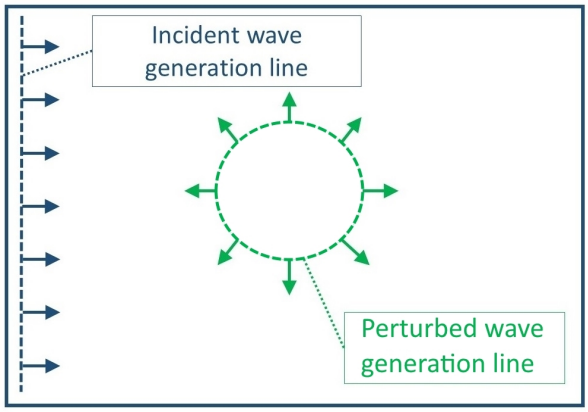

Figure 3: Methodology description sketch.

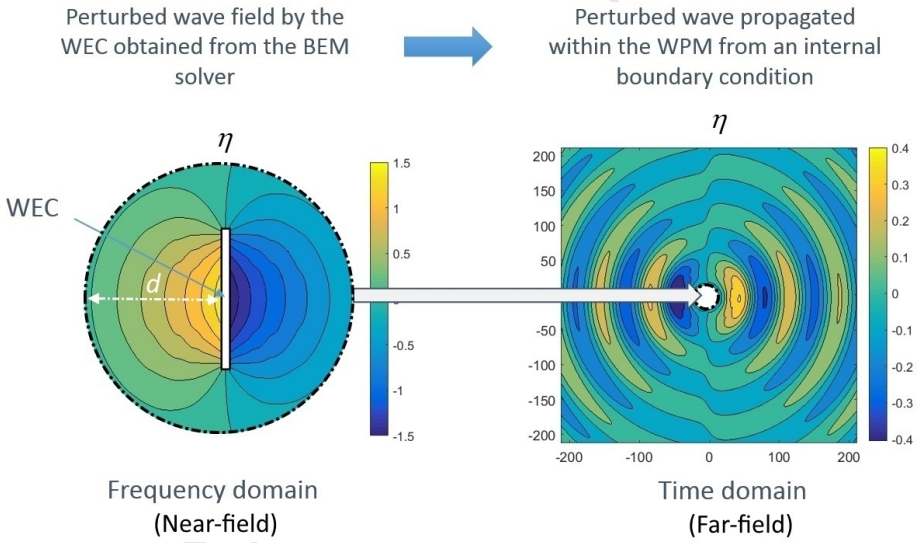

Figure 4: Coupling technique description between the BEM solver and the WPM.

boundary location, i.e. along all grid cells defining the wave generation line. Subscripts N refer to variables obtained from NEMOH and subscripts MW refer to variables imposed in MILDwave. Due to the computational time-staggering in MILDwave between η and Φ, the solution for both variables is imposed with half a time step difference:

$$\eta_{MW}((n+\frac{1}{2})\Delta t) = A_N(\omega)\cos(\varphi_N(\omega) - \omega((n+\frac{1}{2})\Delta t)) \tag{20}$$

ACCEPTED MANUSCRIPT

$$\Phi_{MW}((n+1)\Delta t) = \frac{g}{\omega} A_N(\omega) \sin(\varphi_N(\omega) - \omega((n+1)\Delta t)) \tag{21}$$

The size and shape of the internal boundary can be adapted to the geometry of the WEC farm under consideration, even though a minimum margin distance d of 15 m is recommended between the boundary and the centre of the closest device (see Section 8.4). The mandatory requirement is that the line describing the internal boundary needs to surround completely the WEC farm in order to represent the complete wave energy flux of the perturbed wave.

6. Application to a Single WEC Case

6.1. Comparison between MILDwave and NEMOH

The methodology was first applied to a single WEC case and constant water depth conditions for validation purposes. Since BEM solvers only consider constant water depth conditions the comparison needs to be done under these conditions. The aim of this comparison is to validate that the same perturbed wave from the BEM solver can be reproduced within the WPM with high accuracy applying the coupling technique by means of an internal boundary. Figure 5 shows the comparison between the wave field results obtained intrinsically in NEMOH (left) and by applying the coupling methodology in MILDwave (right) for the same domain. The results represent the perturbed wave field solution corresponding to an incident wave period T of 8 s and amplitude A of 1 m across a domain of 400 x 400 m. The wave results are plotted in terms of wave amplitude and wave phase (frequency domain variables) for both solvers results in order to facilitate the comparison between the frequency domain results from NEMOH and the time domain results from MILDwave.

First the perturbed wave field surrounding the single flap is obtained in NEMOH. A circle surrounding the flap delimits the area corresponding to the near-field and far-field (inner and outer domain respectively) and describes the wave generation line in MILDwave as shown in Figure 4. In this case a circle of radius equal to 25 m is used to define the line where the solution from NEMOH is imposed in MILDwave, at the same location with respect to the WEC. The surface elevation and velocity potential are imposed along the generation line at each instant of time and propagated throughout the rest of the domain. The empty disc in the middle of the domain represents the location where the solution is given by NEMOH and thus its outer limit represents the internal boundary.

6.2. Error between MILDwave and NEMOH

Figure 6 shows the percentage error between the perturbed wave field obtained from MILDwave and that obtained from NEMOH, relative to the average wave amplitude along the boundary that delimits the near-field and far-field. The error is calculated based on Equation (22) where A_M is the wave amplitude result from MILDwave, A_N the wave amplitude result from NEMOH, and $\bar{A_N}$

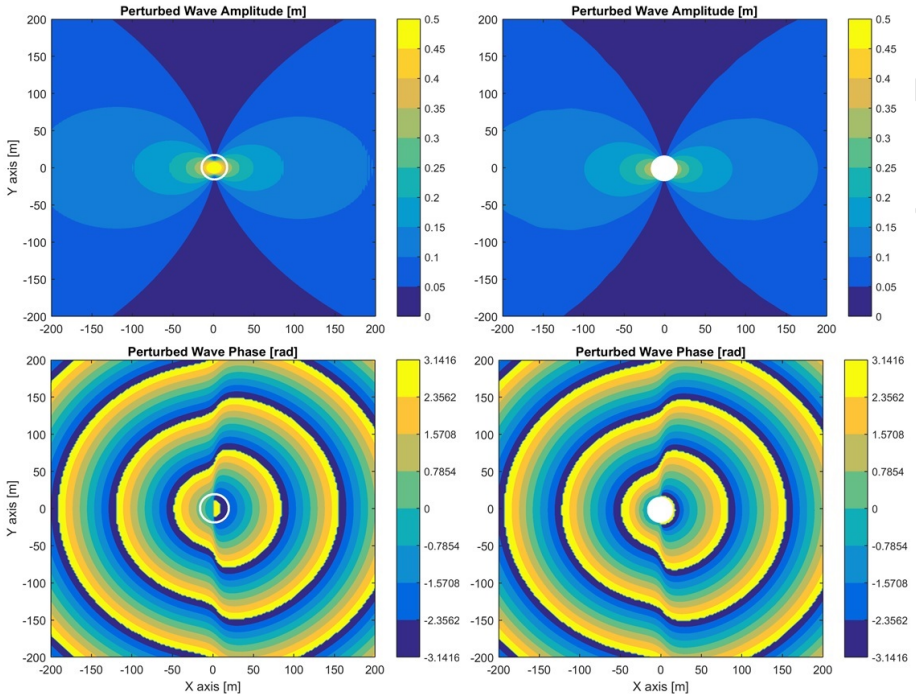

Figure 5: Perturbed wave amplitude and phase obtained in NEMOH (left) and MILDwave (right) for a single flap.

the mean value of the wave amplitudes obtained from NEMOH all along the boundary line. The results from NEMOH are considered here as a target solution and the comparison is possible due to the constant water depth assumptions of this case scenario.

$$\epsilon(\%) = \frac{A_N - A_M}{\bar{A_N}} \tag{22}$$

A small error is present across the $Y = 0$ section with overall error values remaining below 4%. Outside this section the error is less than 1%. The error is relatively larger across the $Y = 0$ section zone since the wave amplitude values are larger at this location. The error remains very small and well within acceptable values considering that the maximum percentage error of 4% corresponds to an absolute difference of 0.0036 m, as the average perturbed wave amplitude $\bar{A_N}$ is equal to 0.09 m.

7. Application to a WEC Farm Case

In this section the methodology is applied to a farm of 5 flaps. The farm is composed of two rows, an up-wave row with 3 flaps and a down-wave row

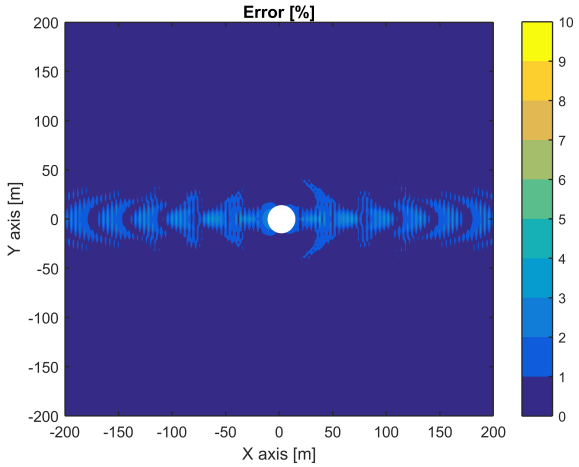

Figure 6: Percentage error between MILDwave and NEMOH results for a single flap

with 2 flaps as illustrated in Figure 7. The lateral spacing between devices S is 40 m and the spacing between rows R is 40 m. The down-wave row of flaps is staggered and placed in front of the gaps from the up-wave row.

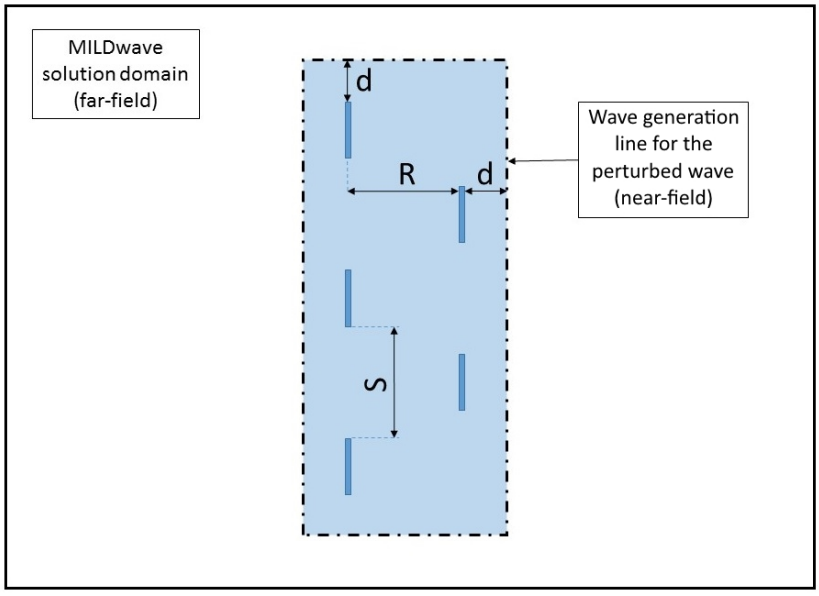

Figure 7: Sketch of the 5 flaps WEC farm layout and the rectangular boundary.

7.1. Comparison between MILDwave and NEMOH

The same incident wave conditions ($T = 8\ s$ and $A = 1\ m$) and constant water depths as previously outlined are considered. In this case the shape of the near-field is a rectangle that fits the form of the WEC farm by leaving a margin distance d of 15 m between the boundary and the centre of the closest device. The dimensions of the rectangle are $60 \times 160\ m$ (X and Y axis respectively). The perturbed wave solution considering all interactions was computed in NEMOH and was then inserted into MILDwave by means of wave generation line of rectangular shape surrounding the near-field. In this case the perturbed wave field from NEMOH was obtained from the superposition of the diffracted wave and the 5 radiated waves corresponding to the motion of each WEC.

Figure 8 shows the perturbed wave amplitude and phase obtained in NEMOH (left) and MILDwave (right) for the 5 flaps case. The same domain size is used again in order to validate the results with the target perturbed wave obtained from NEMOH assuming constant water depths. A rectangle delimits the near-field and far-field area and describes the location of the boundary between the two solvers. Again, the rectangle is empty for the MILDwave calculation since the near-field solution is given by the results obtained with NEMOH.

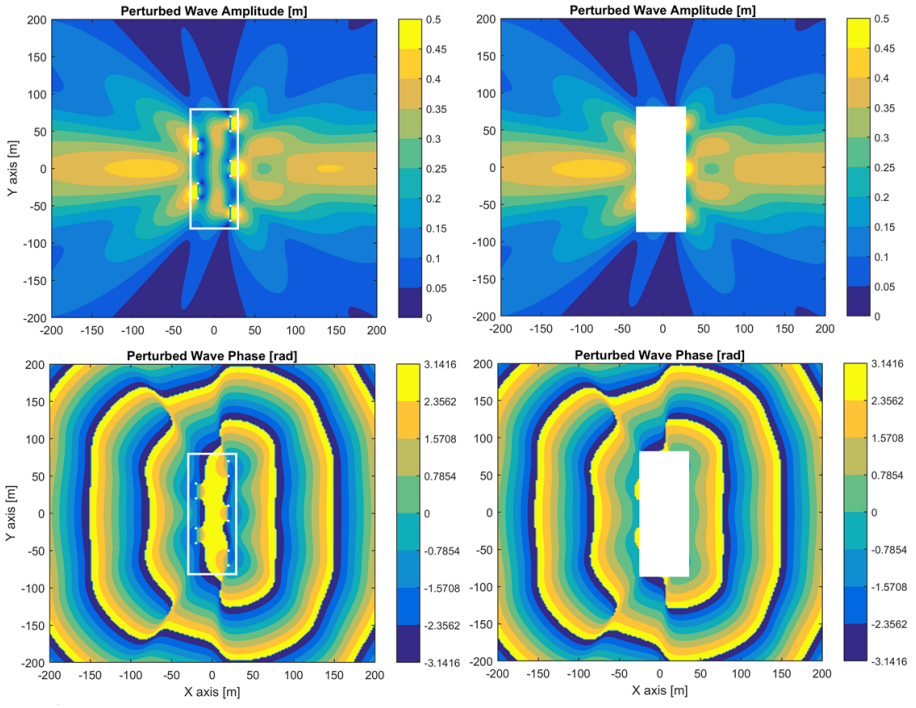

Figure 8: Perturbed wave amplitude and phase obtained NEMOH (left) and MILDwave (right) for 5 flaps.

ACCEPTED MANUSCRIPT

7.2. Error between MILDwave and NEMOH

The percentage error between the perturbed wave obtained from MILDwave and from NEMOH is shown in Figure 9 along the whole domain. The maximum error appears along section $Y = 0$ with values remaining below 2%. Again the error is larger along this section due to the fact that in this zone the perturbed wave amplitude values are the largest in the domain. The error is small considering a percentage error of 2% corresponds to an absolute difference of 0.0055 m, as in this case the mean wave amplitude $\bar{A_N}$ along the boundary corresponds to 0.27 m. Therefore, a very good agreement is found for both applications of the coupling technique, i.e. the single flap case and the 5 flaps case.

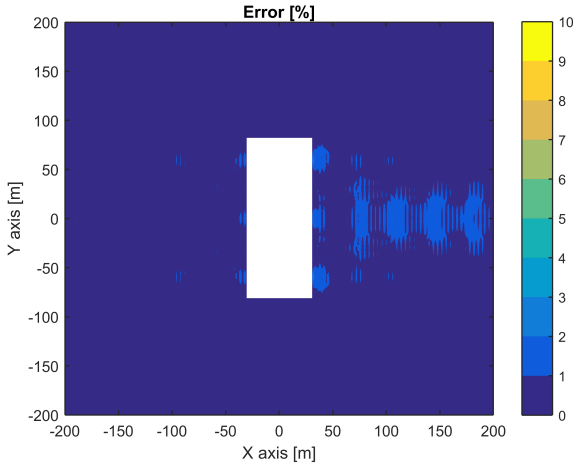

Figure 9: Percentage error between MILDwave and NEMOH results for 5 flaps.

This application case shows the flexibility of the methodology to adapt the near-field area to the shape of the WEC farm. Whether described by a circular or a rectangular shape the internal boundary allows the computation of the perturbed wave in MILDwave with very good agreement.

8. Convergence Analyses

Prior to the calculations from Sections 6 and 7 convergence analyses were carried out in order to investigate the optimal values of the main numerical parameters involved in the coupling methodology, i.e. grid cell size, time step, wave length limits, and near-field area size. Based on the results from the analyses optimal values were assigned to these parameters in order to find the best match in the comparison between MILDwave and NEMOH. These analyses were carried out based on the single flap case study from Section 6.

In the following section the details of the analyses are presented in terms of percentage error with respect to the target values from NEMOH. The error is

calculated by replacing the dividing term $\bar{A_N}$ from Equation (22) by the incident wave amplitude A_i (equal to 1) in order to simplify the comparison between the different analyses. The error values shown in the plots from Sections 8.1, 8.2, 8.3, and 8.4, represent the maximum error obtained along the domain of 400 x 400 m. The computational cost was not included in the convergence analysis since all calculations remain under a very low simulation cost, of the order of seconds for the cases considered in this section. Therefore at this stage of the methodology development the priority was given to the error decrease.

8.1. Time step

The reference time step value given by the MILDwave developers in order to ensure a stable computation is $\Delta t \leq \Delta x/C$ [27] which represents the Courant-Friedrichs-Lewy criterion. Based on this reference, several cases were run for values of $\Delta t = 0.02\Delta x/C$ to $\Delta t = \Delta x/C$ considering the same regular wave of $A = 1\ m$ and $T = 8\ s$ from previous sections. However above values of $\Delta t = 0.65\Delta x/C$ the calculations became unstable and could not be achieved. The results obtained from the analysis are shown in Figure 10 where the lowest error obtained was 0.36% remaining relatively constant for all values between $\Delta t = 0.1\Delta x/C$ and $\Delta t = 0.65\Delta x/C$.

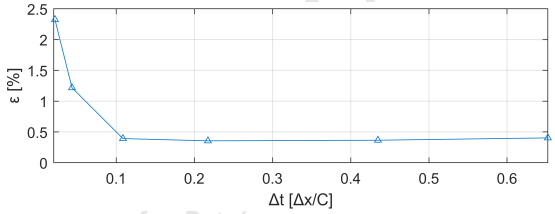

Figure 10: Maximum error vs. time step.

8.2. Grid cell size

In the case of the grid cell size the reference values for MILDwave are $\lambda/20 \leq \Delta x \leq \lambda/10$ [27] for non-breaking waves where λ represents the wave length. These values are based on deep water conditions therefore a shift in the recommended range towards lower values can be found when considering shallow water conditions as in the case of this work. In this analysis cases were run for values of $\Delta x = \lambda/140$ to $\Delta x = \lambda/8$ where the same regular wave of $A = 1\ m$ and $T = 8\ s$ was considered. The convergence was obtained for values lower than $\Delta x = \lambda/30$, reaching the minimum error of 0.36% and remaining constant until $\Delta x = \lambda/140$.

8.3. Wave length

Following the same reference of $\lambda/20 \leq \Delta x \leq \lambda/10$ for the ratio between the wave length and grid cell size, an analysis of the influence of the wave length on

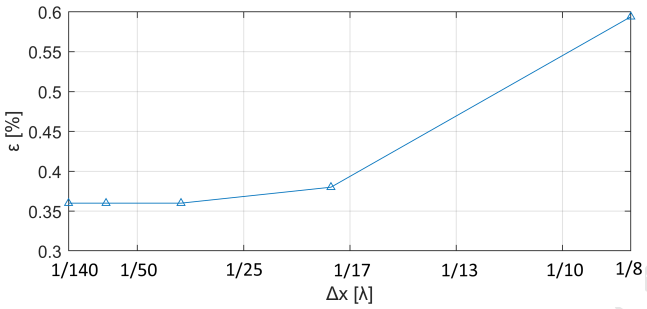

Figure 11: Maximum error vs. grid cell size.

the error was carried out considering a fixed grid cell size. The results obtained are shown in Figure 12. In this case the error fluctuates considerably due to the influence of the absorption layers at the up-wave and down-wave boundaries of MILDwave that are adjusted in width for each wave period. A convergence was still achieved around values with an average error of 0.8% located between $\lambda = 20\Delta x$ and $\lambda = 90\Delta x$. The lowest error of 0.36% was found for values close to $\lambda = 35\Delta x$ and this is considered to be the optimal case.

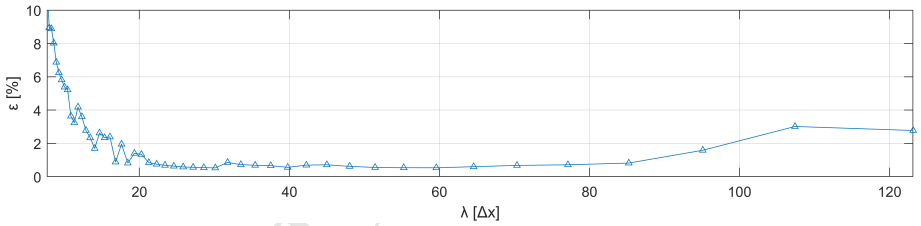

Figure 12: Maximum error vs. wave length.

This analysis proved the importance of considering the wave lengths limits (and therefore wave frequency limits) that can be used with the same grid cell size when running sea states characterised by many different wave frequencies. In the case of irregular sea states composed of a superposition of regular waves, a fixed grid cell size can be applied to a all frequencies if the correct grid cell size is chosen so that all results remain under an error of 1%. This is achievable if the Δx and Δt are chosen to be optimum for the wave length corresponding to the peak wave period T_p of the sea state.

8.4. Near-field area size

Here a convergence analysis for the size of the near-field area enclosed by the boundary was achieved in order to find the smallest area that provides a good agreement. The margin distance d, defined as the shortest distance between a

ACCEPTED MANUSCRIPT

device and the boundary, was changed for each case from $d = \lambda/35$ to $d = \lambda/2$. The error clearly converges as d increases reaching an optimum value at $d = \lambda/5$ as shown in Figure 13. Thus, a minimum margin distance $d = \lambda/5$ needs to be left when defining the size of the near-field area in order to maximise the accuracy of this coupling technique. However, lower values of d are acceptable as well since the error remain below 1% for all cases. It is important to notice that the area corresponding to the near-field in MILDwave assumes constant water depth conditions and thus the interest on keeping its size as reduced as possible.

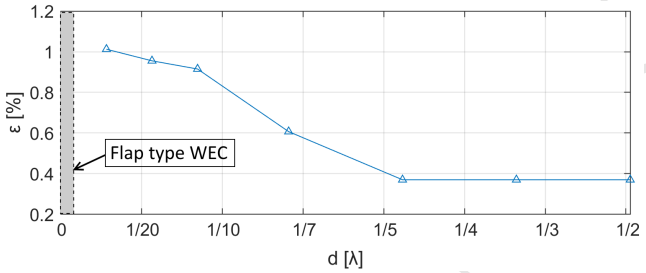

Figure 13: Maximum error vs. near-field area size.

9. Wake Effect Assessment for a WEC Farm

The wake effect for a farm composed of 18 flaps was computed in this section using a large domain, irregular long crested waves, and a mild-slope bathymetry. The aim is to demonstrate step by step the calculations carried out to assess the wake effect for a realistic WEC farm case scenario. A domain of 1500 x 3000 m (Y and X axis respectively) was chosen as it gives a greater scope to assess the wake effect in the far-field.

In this case the WEC farm is composed of 4 rows where the first and third row are composed of 4 flaps and the second and fourth of 5 flaps as shown in Figure 14. The lateral spacing between devices S and spacing between rows R are 100 m and 44 m respectively. The spacings S and R were defined based on the assessment carried out in a previous publication [7] where the WEC farm layout was chosen based on the available wave energy resources, i.e. wave energy density. The centre of the WEC farm is located along section $X = -500$ m and centred with respect to the Y axis at a water depth h of 10 m, which is the constant water depth assumed for the near-field solution in NEMOH.

The farm is located on a changing bathymetry which is defined by a linear mild-slope with the depth decreasing towards the X positive axis direction, the same direction than the wave propagation direction. The bathymetry profile ranges in water depths between 12 and 6 m with a small section where constant water depths are assumed for the WEC farm location as shown in Figure 15.

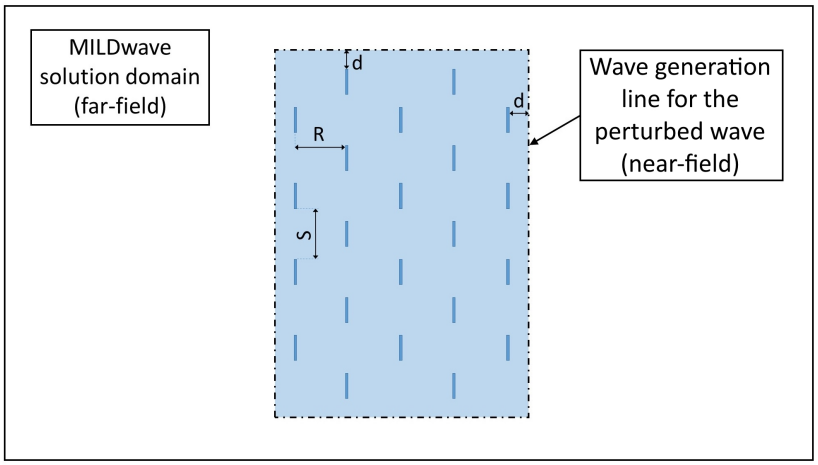

Figure 14: Sketch of the 18 flaps WEC farm layout and the rectangle boundary.

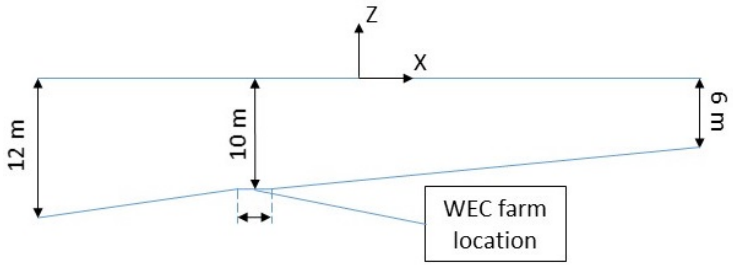

Figure 15: Mild-slope bathymetry profile.

9.1. Regular waves

Irregular long crested waves are calculated as a sum of the regular waves that compose the sea state, based on the superposition principle from linear water wave theory. The first step is to calculate the total wave amplitude for each regular wave across the whole domain. Each total wave is composed of an incident wave propagated in an empty domain (absence of WEC farm) calculated intrinsically in MILDwave and a perturbed wave created by the presence of the WEC farm obtained by means of the coupling technique. The perturbed wave is computed based on the amplitude and phase of the incident wave solution at the centre of the WEC farm.

Figure 16 shows the incident, perturbed, and total wave amplitude for an example of a regular wave of $T = 8\ s$ and $A = 1\ m$ on a mild-slope bathymetry. For the case of the perturbed wave plot, the near-field and far-field results are shown together, proving there is no discontinuity between the domain solved by

NEMOH and the domain solved by MILDwave.

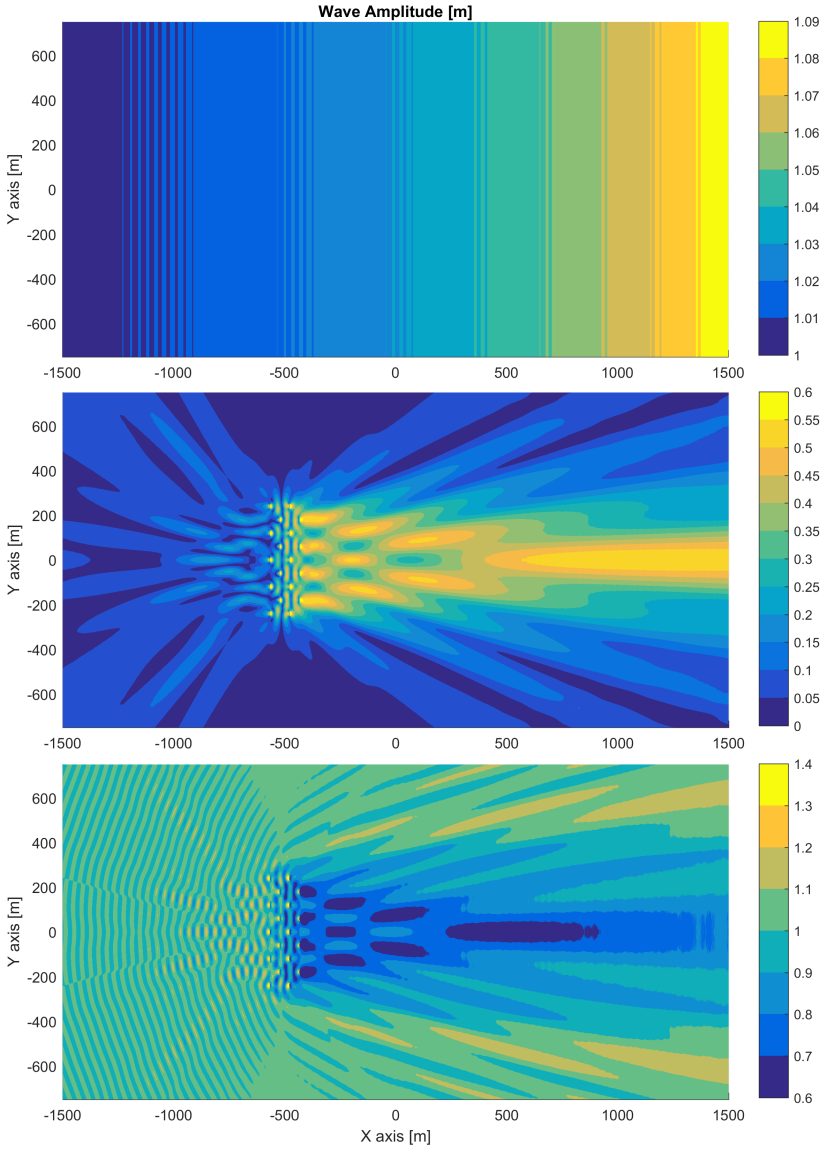

Figure 16: Incident (absence of WEC farm), perturbed (presence of WEC farm), and total wave amplitude for a 18 flaps farm on a mild-slope bathymetry.

9.2. Irregular waves

Given a specific incident irregular sea state, the local changes in the wave spectral density can be obtained for each grid cell along the domain based on

the regular wave solutions. The relation between the wave spectral density and the total wave amplitude for each frequency interval is defined by Equation (23) which allows the determination of the spectral density distribution of the sea state along the frequency range. A range of 50 regular frequencies have been used in this work to discretise the irregular sea states.

$$S(\omega)\Delta\omega = \frac{1}{2}A^2(\omega) \tag{23}$$

The wave spectral density S changes along the domain with the water depth h and with the disturbance generated by the WEC farm. Thus, in order to assess the WEC farm disturbance the spectral density distribution is obtained for the undisturbed sea state S_u, in the absence of the WEC farm, and then for the disturbed sea state S_d, in the presence of the WEC farm. In the case of the undisturbed sea state the wave amplitude A corresponds to the incident wave amplitudes for each wave frequency and in the case of the disturbed sea state it corresponds to the total wave amplitude. Figure 17 shows an example of the change in the wave spectral density due to the presence of a WEC farm for a grid cell centrally located 150 m down-wave of the farm ($X = -350$ m and $Y = 0$ m). From the significant wave height for S_u and S_d the WEC farm disturbance is quantified by the disturbance coefficient K_d described by Equation (24).

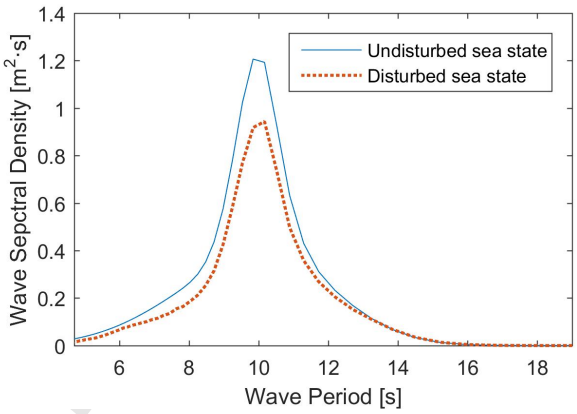

Figure 17: Wave spectral density disturbance at a grid cell point located in the lee side of the farm for irregular waves.

$$K_d = \frac{H_{Sd}}{H_{Su}} \tag{24}$$

where H_{Sd} and H_{Su} are the significant wave height for the disturbed and undisturbed sea state respectively at each grid cell of the numerical domain.

The disturbance coefficient can be now obtained for the whole domain to evaluate the disturbance generated by the WEC farm on the surrounding wave

ACCEPTED MANUSCRIPT

field (so-called wake effect). Figure 18 shows the disturbance coefficient K_d for three incident sea states of peak periods (T_p) of 8 s, 10 s, and 12 s, and significant wave height (H_s) of 2 m. However, due to the linear wave theory assumptions the K_d value is not dependent on the significant wave height and the incident sea state is defined here only by the peak period. The PTO system of each flap has been tuned for every sea state according to Equation (19) based on the peak angular wave frequency ω_p.

The wake effect for the studied WEC farm shows a large wave height decrease behind the WEC farm that persists into the far field at least until 2 km downwave from the farm. A large difference is found between the different sea states due to the wave energy absorption capacity of the WECs. The WECs power extraction reaches a saturation at certain sea states depending mainly on the dimensions of the device, instead of keep increasing with the higher energy sea states. Thus, for the same WEC farm power absorption, the higher the peak period is the less pronounced is the decrease in the disturbance coefficient.

The flap type device was modelled as it is one of the technologies that most affects the incoming wave field. Due to its vertical orientation the device extends through the full water column and acts as a submerged moving barrier. Therefore the wave height reduction is expected to be more significant than for other WEC technologies.

Considering an area in the lee-side of the WEC farm from a minimum distance of 500 m ($X = 0$ m) behind the farm and up to the far-field, the lowest K_d values are found for the sea state of $T_p = 8$ s with minimum values around 0.65 (equivalent to 35% of significant wave height reduction) and average values varying between 0.85 and 0.65 (15% and 35% reduction, respectively). The reduction effect progressively decreases with increasing the peak period, with values ranging between 30% and 10% of reduction for $T_p = 10$ s, and between 25% and 10% of reduction for $T_p = 12$ s. If a larger distance was considered in the lee-side of the farm the K_d values will progressively increase towards far-field reaching eventually at a certain point values equal to 1, meaning that the wave energy flux recovers because of diffraction.

10. Influence of the WEC Lateral Spacing

The lateral spacing between the WECs of the farm (S) is a significant parameter in terms of the wake effect since it affects the interactions between WECs and thus their wave energy absorption. The larger the lateral spacing is the less each WEC is influenced by the surrounding WECs and therefore the WECs dynamics will be closer to the case of an isolated WEC. Also the diffraction phenomenon is significantly affected by the spacing between WECs, which is quantified by the ratio between the wave length corresponding to the peak period and the shortest lateral spacing between WECs. Thus, changing the lateral spacing can lead to significant differences in the WEC farm wake effect.

Figure 19 shows the disturbance coefficient K_d obtained for a WEC farm composed of 9 flaps in a single row where S was set to $4L$, $5L$, and $6L$ (L equal

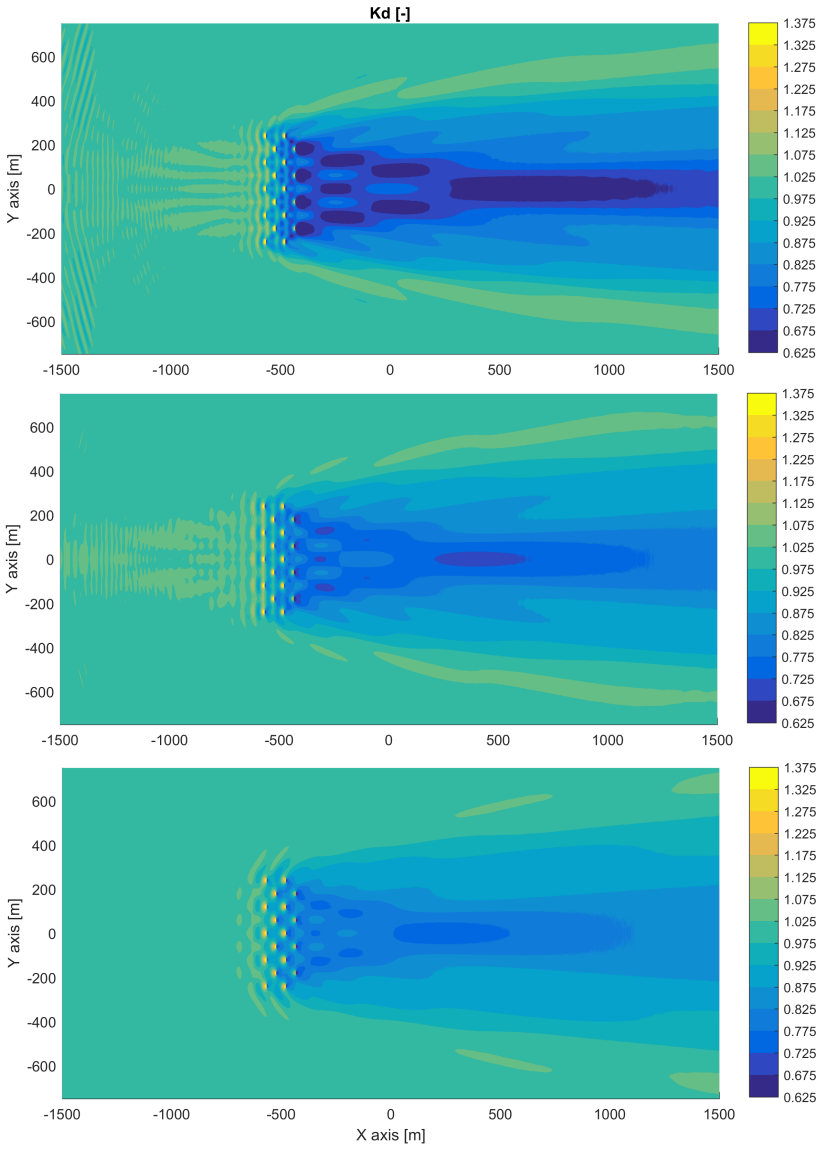

Figure 18: Disturbance coefficient for a 18 flaps farm on a mild-slope bathymetry for sea states of T_p equal to 8 s, 10 s, and 12 s (from top to bottom).

to the WEC length) respectively (top to bottom) and a sea state of T_p equal to 8 s. The same mild-slope bathymetry as shown in Figure 18 was used but the average K_d values obtained in the farm lee-side are smaller since the number of devices and rows is reduced. It is clear that the lateral spacing affects the wave

height reduction behind the farm. As expected, the larger the WEC lateral spacing is, the lower is the wave height decrease in the lee-side of the WEC farm. The area in the lee-side of the farm corresponding to K_d values ranging between 0.875 and 0.925 (12.5% and 8.5% wave height reduction respectively) becomes progressively reduced in size by increasing the lateral spacing S and it nearly disappears for the case of $S = 6L$.

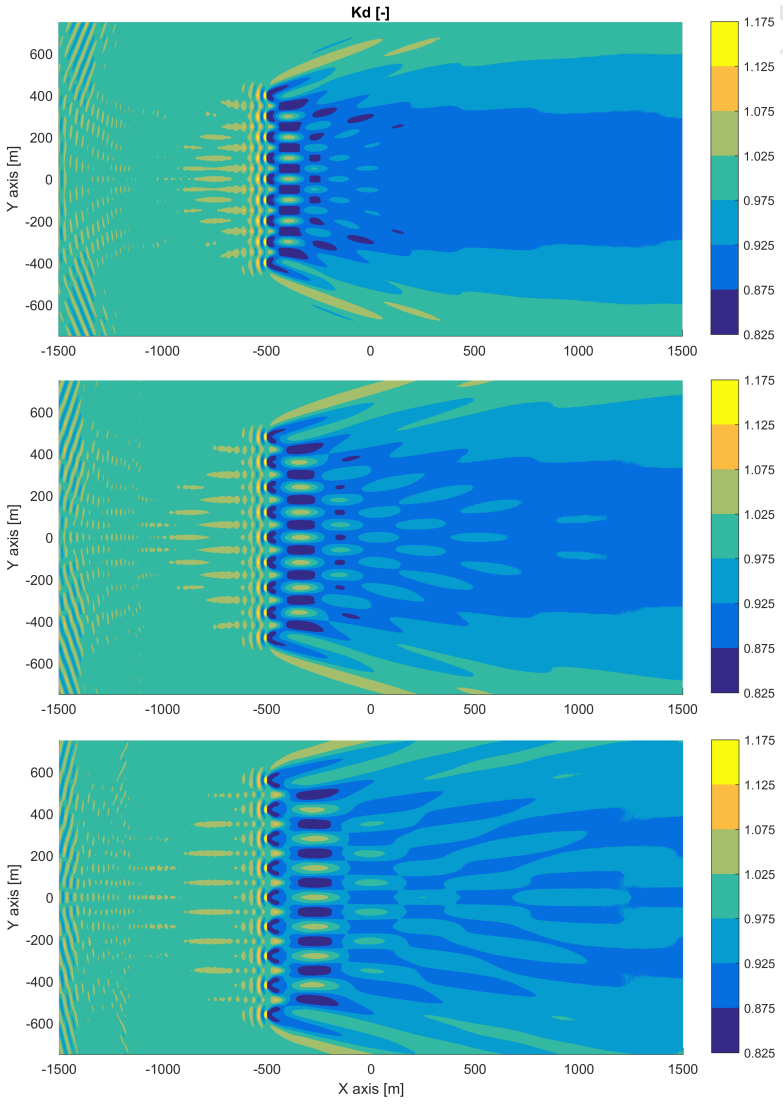

Figure 19: Disturbance coefficient for spacings of $4L$, $5L$, and $6L$ respectively (top to bottom) and sea state of T_p equal to 8 s.

11. Real Case Scenario with Irregular Bathymetry

A realistic bathymetry scenario was considered in this section to demonstrate the applicability of the methodology. The bathymetry corresponds to a near-shore area located off Annagh Head, west of Belmullet (Ireland) near the Atlantic Marine Energy Test Site (AMETS). Figure 20 shows a detailed map of the site (top) where the highlighted rectangular section of 500 x 1000 m defines the area corresponding to considered bathymetry and the general map of Ireland (bottom) shows the location of the AMETS site. The bathymetry data was obtained from the Integrated Mapping For the Sustainable Development of Irelands Marine Resource (INFOMAR) programme through their data acquisition platform [39].

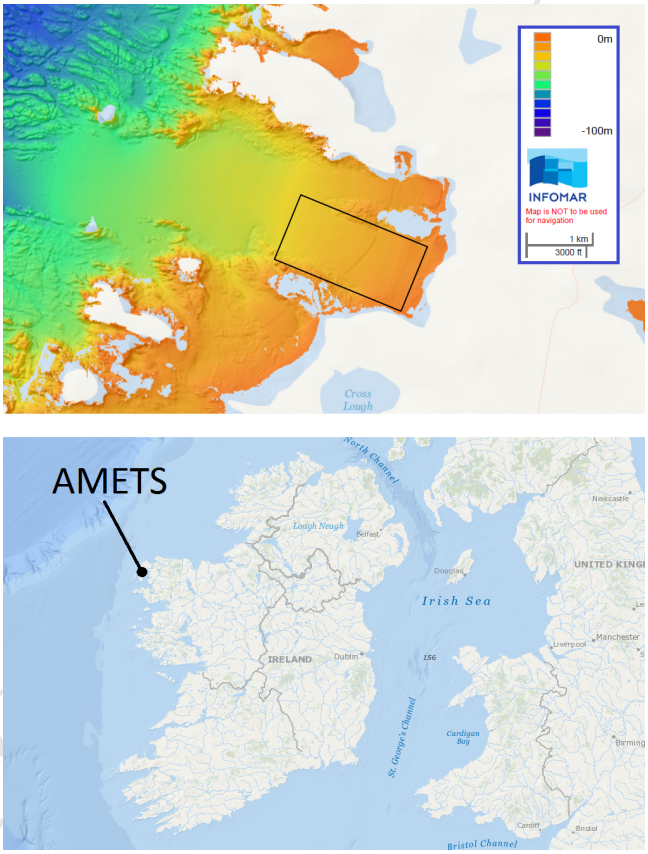

Figure 20: Detailed map of AMETS region with the bathymetry area highlighted (top). General map of Ireland with AMETS location (bottom).

The same WEC farm configuration of 18 flaps was considered but this time deployed at a water depth of 15 m. The flaps are submerged 3 m below the

ACCEPTED MANUSCRIPT

water surface and this reduces their impact on the surrounding wave field. For the site selection it was considered that a minimum distance of 1 km away from the shore was necessary to avoid any problems with near-shore marine activities. In addition, a large area with similar water depth values is necessary for the installation of the WEC farm.

Figure 21 shows the water depth values (top), the K_d values across the whole domain (middle), and the K_d difference compared to a constant water depth scenario where the same conditions for the WEC farm are considered (bottom). An incident sea state of $T_p = 8\ s$ was considered at the offshore boundary representing the sea state with the highest occurrence in a year for the AMETS site. For the comparison with the constant water depth case the wave spectral distribution and the water depth were chosen to be the same at the location of the WEC farm, eventually generating a similar wave disturbance on the incoming sea state and where the K_d differences are only due to the different bathymetries.

The lowest K_d values found on the lee-side of the farm are about 0.85 at specific locations. On average the wave height reduction remains around 10%, which proves that for this case scenario the impact of the WEC farm on the surrounding wave climate and near-shore remains low. If a farm composed of surface-piercing flaps such as the one presented in Section 9 was considered, the impact would be significantly larger. The bottom plot of Figure 21 shows that differences up to 10% are found for this case scenario, proving the importance of representing real bathymetries when assessing wake effects. Again, if a farm of surface-piercing flaps was considered the difference would be even larger. The asymmetric pattern of the results is a proof as well of the high influence of the bathymetry in the WEC farm wake effect.

12. Conclusion

This work has detailed the working principle of a numerical coupling methodology between the wave near-field solution obtained from a Boundary Element Method (BEM) solver and the wave far-field solution from a Wave Propagation Model (WPM). The BEM solver provides with the solution of the perturbed wave field from the WEC farm that is described as an internal boundary within the WPM and then propagated throughout the rest of the domain. The internal boundary consists on a group of grid cells defining a wave generation line where the results from the BEM solver at the same location are imposed at each time step. The solution obtained for the perturbed wave field is then superposed to the incident wave field obtained in the absence of WEC farm in order to obtain the total wave field for each regular wave frequency. Finally, irregular sea states are composed based on the total wave field results from the regular waves ranging within the wave spectral density distribution of the considered sea state.

The presented approach has demonstrated to give highly accurate results when comparing the results to the target solutions from the BEM solver. The

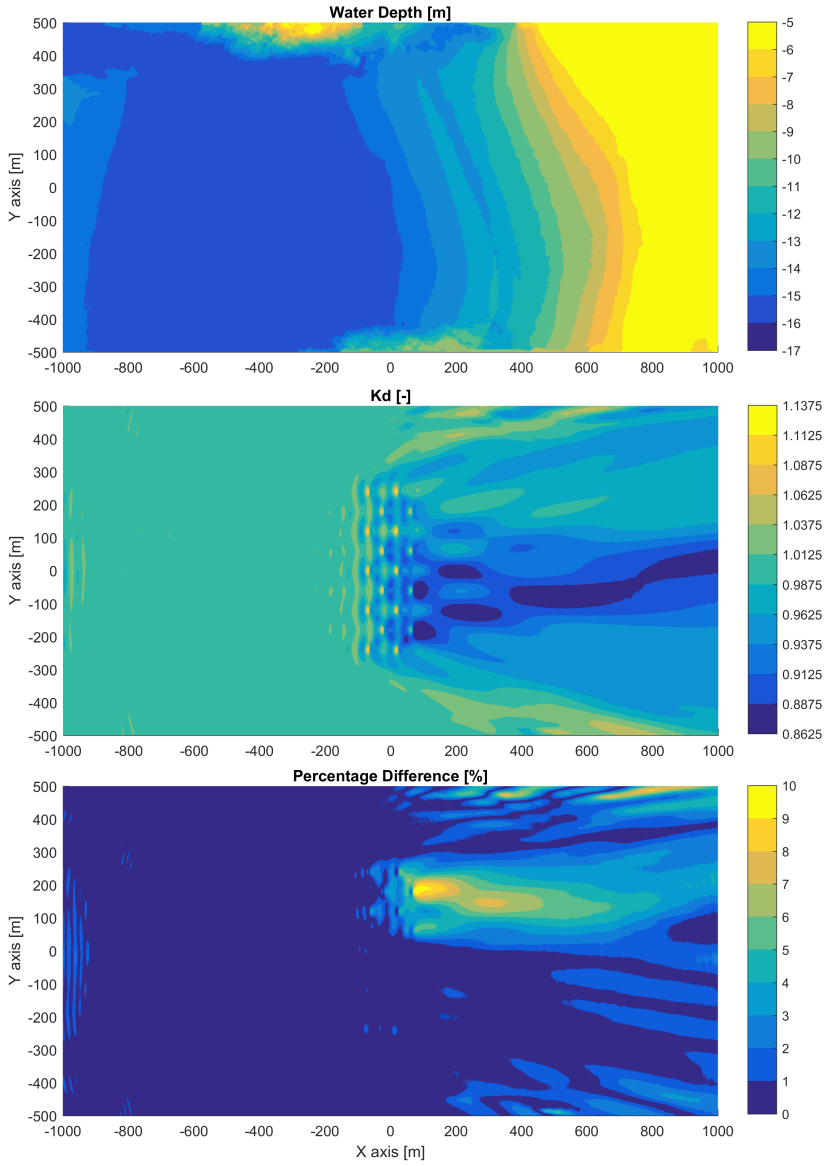

Figure 21: Water depth across bathymetry (top). Disturbance coefficient for 18 flaps on a real bathymetry considering a sea state of $T_p = 8\ s$ (middle). Percentage difference with a constant water depth scenario (bottom).

technique has proven to be versatile by adapting the internal boundary in MILD-
655 wave to the shape and size of the WEC farm. This allows the reduction of the area where the limitations of the BEM solvers are assumed (constant water

ACCEPTED MANUSCRIPT

depths). A convergence analysis for the main numerical parameters influencing the results was undertaken in order to investigate the range of optimal values to be used. This was followed by a sensitivity analysis where the influence of the peak period and the lateral WEC lateral spacing on WEC farm wake effects was assessed. Finally, the wake effect for a 18 flaps WEC farm exposed to irregular long crested waves at a real site was assessed in order to demonstrate the capacity of the methodology to consider real site conditions.

The methodology relies on the linear water wave theory assumptions that remain valid in most of the operational sea state conditions. For the case of sea states where non-linearities become important, higher order wave-structure interaction solvers and wave propagation models are needed. However the implementation of these solvers will increase the demand in computational time making the computation of large domains such as those considered in this study not feasible by using standard computers. A way to increase the accuracy of the methodology for highly non-linear sea states is to add linear dissipation coefficients to the main governing equations as it was done in [16] to represent wave breaking and in [10] to represent wave regeneration due to the action of wind.

The proposed numerical coupling methodology remains relatively fast in terms of computational time. A limitation in the computational time can occur when obtaining the near-field within the BEM solver for extremely large WEC farms since computing all wave interactions can be computationally demanding. However, currently it is the most practical way for computing all wave interactions within a farm of WECs. New methodologies are under development to compute wave interactions between WECs based on cylindrical solutions of the perturbed velocity potential from BEM solvers [40, 12]. These methodologies can decrease significantly the calculation time of the perturbed wave for a large WEC farm and constant water depths conditions.

The methodology has shown that large WEC farms can have a significant impact on the wave field. Thus it will be important to assess this impact as part of the consenting process for the environmental impact assessment procedure for future commissioning of WEC farms. The development of coupling methodologies such as the one demonstrated in this work will allow the wake effects to be estimated with a much higher precision than with previous methodologies where WECs were represented as obstacle cells or source terms. The methodology enables the quantification of the sheltering effect of a WEC farm and thus to evaluate its impact on the near-shore and the possible synergies with other marine activities sharing the surrounding sea space.

Acknowledgement

The research leading to these results is part of the OceaNET project, which has received funding from the European Union's Seventh Framework Programme for research, technological development and demonstration under grant agreement no 607656. This research has also been supported by the Research Foundation Flanders (FWO), Belgium, Research Project no. 3G029114.

ACCEPTED MANUSCRIPT

References

[1] C. Beels, P. Troch, G. De Backer, M. Vantorre, J. De Rouck, Numerical implementation and sensitivity analysis of a wave energy converter in a time-dependent mild-slope equation model, Coastal Engineering 57 (5) (2010) 471–492. doi:10.1016/j.coastaleng.2009.11.003.

[2] C. Beels, P. Troch, K. De Visch, J. P. Kofoed, G. De Backer, Application of the time-dependent mild-slope equations for the simulation of wake effects in the lee of a farm of Wave Dragon wave energy converters, Renewable Energy 35 (8) (2010) 1644–1661. doi:10.1016/j.renene.2009.12.001.

[3] H. C. M. Smith, C. Pearce, D. L. Millar, Further analysis of change in nearshore wave climate due to an offshore wave farm: An enhanced case study for the Wave Hub site, Renewable Energy 40 (1) (2012) 51–64. doi:10.1016/j.renene.2011.09.003.

[4] R. Carballo, G. Iglesias, Wave farm impact based on realistic wave-WEC interaction, Energy 51 (2013) 216–229. doi:10.1016/j.energy.2012.12.040.

[5] M. Veigas, V. Ramos, G. Iglesias, A wave farm for an island: Detailed effects on the nearshore wave climate, Energy 69 (2014) 801–812. doi:10.1016/j.energy.2014.03.076.

[6] J. Abanades, D. Greaves, G. Iglesias, Coastal defence using wave farms: The role of farm-to-coast distance, Renewable Energy 75 (2015) 572–582. doi:10.1016/j.renene.2014.10.048.

[7] N. Tomey-Bozo, J. Murphy, P. Troch, T. Lewis, G. Thomas, Modelling of a flap-type wave energy converter farm in a mild-slope equation model for a wake effect assessment, IET Renewable Power Generation (2017) 1–11doi:10.1049/iet-rpg.2016.0962.

[8] J. C. Mcnatt, A. Porter, K. Ruehl, J. Roberts, Verification of the SNL-SWAN Spectral WEC-wave Model with Phase-resolved Linear Wave Fields, in: 12th European Wave and Tidal Energy Conference, Cork, Ireland, 2017, pp. 1–10.

[9] G. Verao Fernandez, P. Balitsky, N. Tomey-Bozo, V. Stratigaki, P. Troch, Far-field effects by arrays of oscillating wave surge converters and heaving point absorbers: a comparative case study, in: 12th European Wave and Tidal Energy Conference, Cork, Ireland, 2017.

[10] V. Stratigaki, P. Troch, L. Baelus, Y. Keppens, Introducing wave generation by wind in a mild-slope wave propagation model MILDwave, to investigate the wake effects in the lee of a farm of wave energy converters, in: 30th International Conference on Ocean, Offshore and Arctic Engineering, Rotterdam, The Netherlands, 2011, pp. 429–436.

ACCEPTED MANUSCRIPT

[11] B. Borgarino, A. Babarit, P. Ferrant, Impact of wave interactions effects on energy absorption in large arrays of wave energy converters, Ocean Engineering 41 (2012) 79–88. doi:10.1016/j.oceaneng.2011.12.025.

[12] J. C. Mcnatt, V. Venugopal, D. Forehand, A novel method for deriving the diffraction transfer matrix and its application to multi-body interactions in water waves, Ocean Engineering 94 (2014) 173–185. doi:10.1016/j.oceaneng.2014.11.029.

[13] M. Folley, A. Babarit, B. Child, D. Forehand, L. O'Boyle, K. Silverthorne, J. Spinneken, V. Stratigaki, P. Troch, A Review of Numerical Modelling of Wave Energy Converter Arrays, in: ASME 2012 31st International Conference on Ocean, Offshore and Arctic Engineering, Rio de Janeiro, Brazil, 2012, pp. 535–545. doi:10.1115/OMAE2012-83807.

[14] M. Folley, Numerical Modelling of Wave Energy Converters: State-of-the-Art Techniques for Single Devices and Arrays, Academic Press, 2016.

[15] C. Beels, Optimization of the Lay-Out of a Farm of Wave Energy Converters in the North Sea. Analysis of Wave Power Resources, Wake Effects, Production and Cost, Ph.D. thesis, Ghent University (2009).
URL https://biblio.ugent.be/publication/978565/file/4335143.pdf

[16] V. Stratigaki, Experimental study and numerical modelling of intra-array interactions and extra-array effects of wave energy converter arrays, Ph.D. thesis, Ghent University (2014).
URL https://biblio.ugent.be/publication/5664337/file/5664342.pdf

[17] A. Babarit, M. Folley, F. Charrayre, C. Peyrard, M. Benoit, On the modelling of WECs in wave models using far field coefficients, in: 10th European Wave and Tidal Energy Conference, Aalbord, Denmark, 2013.

[18] F. Charrayre, C. Peyrard, M. Benoit, A. Babarit, A coupled methodology for wave-body interactions at the scale of a farm of wave energy converters including irregular bathymetry, in: ASME 2014 33rd International Conference on Ocean, Offshore and Arctic Engineering, San Francisco, USA, 2014, pp. 1–9.

[19] P. Troch, V. Stratigaki, Phase-resolving wave propagation array models, in: M. Foley (Ed.) (Ed.), Numerical modelling of wave energy converters : state-of-the-art techniques for single devices and arrays, Elsevier, 2016, pp. 191—-216.

[20] P. M. Ruiz, F. Ferri, J. P. Kofoed, Water wave diffraction and radiation by three-dimensional bodies over mild slope bottom, Ocean Engineering 143 (May) (2017) 4–5. doi:10.1016/j.oceaneng.2017.08.007.

ACCEPTED MANUSCRIPT

[21] N. Tomey-Bozo, J. Murphy, A. Babarit, P. Troch, T. Lewis, G. Thomas, Wake effect assessment of a flap type wave energy converter farm using a coupling methodology, in: ASME 2017 36th International Conference on Ocean, Offshore and Arctic Engineering, Trondheim, Norway, 2017.

[22] C.-H. Lee, WAMIT theory manual (1995).
URL http://www.wamit.com/

[23] N. Tomey-Bozo, J. Murphy, P. Troch, A. Babarit, T. Lewis, G. Thomas, The modelling of a flap type wave energy converter in a time-dependent mild-slope equation model, in: Renewable Energies Offshore, 2016, pp. 277–284.

[24] P. Balitsky, G. Verao Fernandez, V. Stratigaki, P. Troch, Coupling methodology for modelling the near-field and far-field effects of a wave energy converter, in: 36th International Conference on Ocean, Offshore and Arctic Engineering, Trondheim, Norway, 2017, pp. 1–10.

[25] P. Balitsky, G. Verao Fernandez, V. Stratigaki, P. Troch, Assessing the impact on power production of WEC array separation distance in a wave farm using one-way coupling of a BEM solver and a wave propagation model, in: 12th European Wave and Tidal Energy Conference, Cork, Ireland, 2017, pp. 1176—-1186.

[26] A. Babarit, G. Delhommeau, Theoretical and numerical aspects of the open source BEM solver NEMOH, in: 11th European Wave and Tidal Energy Conference, Nantes, France, 2015.

[27] P. Troch, MILDwave: A numerical model for propagation and transformation of linear water waves, Tech. rep., Department of civil engineering, Ghent University, Ghent (1998).

[28] T. Verbrugghe, P. Troch, A. Kortenhaus, V. Stratigaki, A. Engsig-Karup, Development of a numerical modelling tool for combined near field and far field wave transformations using a coupling of potential flow solvers, in: 2nd International Conference on Renewable energies Offshore, Lisbon, Portugal, 2016, pp. 61–68. doi:978-1-138-62627-0.

[29] T. Verbrugghe, V. Stratigaki, P. Troch, R. Rabussier, A. Kortenhaus, A comparison study of a generic coupling methodology for modeling wake effects of wave energy converter arrays, Energies 10 (11). doi:10.3390/en10111697.

[30] A. P. Engsig-Karup, H. B. Bingham, O. Lindberg, An efficient flexible-order model for 3D nonlinear water waves, Journal of Computational Physics 228 (6) (2009) 2100–2118. doi:10.1016/j.jcp.2008.11.028.
URL http://dx.doi.org/10.1016/j.jcp.2008.11.028

ACCEPTED MANUSCRIPT

[31] T. Verbrugghe, B. Devolder, J. Domínguez, A. Kortenhaus, P. Troch, Feasibility study of applying SPH in a coupled simulation tool for wave energy converter arrays, in: 12th European Wave and Tidal Energy Conference, Cork, Ireland, 2017.

[32] T. Verbrugghe, A. Kortenhaus, P. Troch, J. M. Dominguez, A non-linear 2-way coupling between DualSPHysics and a wave propagation model, in: 12th International SPHERIC Workshop, Ourense, Spain, 2017, pp. 121–127.

[33] G. Delhommeau, Seakeeping codes aquadyn and aquaplus, in: 19th WEGEMT School Numerical Simulation of Hydrodynamics: Ships and Offshore Structures, 1993.

[34] J.-C. Galland, N. Goutal, J.-M. Hervouet, TELEMAC: A new numerical model for solving shallow water equations, Advances in Water Resources 14 (3) (1991) 138–148. doi:10.1016/0309-1708(91)90006-A.

[35] A. Radder, M. Dingemans, Canonical equations gravity waves, weakly non-linear gravity waves, Wave Motion 7 (1985) 473–485.

[36] N. Booij, A note on the accuracy of the mild-slope equation, Coastal Engineering 7 (3) (1983) 191–203. doi:10.1016/0378-3839(83)90017-0.

[37] C. Lee, K. D. Suh, Internal generation of waves for time-dependent mild-slope equations, Coastal Engineering 34 (1-2) (1998) 35–57. doi:10.1016/S0378-3839(98)00012-X.

[38] H. tao Zhao, Z. lin Sun, C. ling Hao, J. fa Shen, Numerical modeling on hydrodynamic performance of a bottom-hinged flap wave energy converter, China Ocean Engineering 27 (1) (2013) 73–86. doi:10.1007/s13344-013-0007-y.

[39] Marine Institute, The INtegrated Mapping FOr the Sustainable Development of Ireland's MArine Resource (INFOMAR).
URL http://www.infomar.ie/

[40] F. Fàbregas Flavià, C. McNatt, F. Rongère, Aurélien Babarit, A. H. Clément, Computation of the Diffraction Transfer Matrix and the Radiation Characteristics in the open-source BEM code NEMOH, in: ASME 2016 35th International Conference on Ocean, Offshore and Arctic Engineering, Busan, South Korea, 2016.